

Study of the Mechanism of Liquid Slag Infiltration for Lubrication in Slab Continuous Casting



SHAODA ZHANG, QIANGQIANG WANG, SHENGPING HE, and QIAN WANG

Consistent and uniform lubrication of the solidifying shell, especially in the meniscus, is crucial for the smooth continuous casting operation and production of strands free of surface defects. Thus, the current study established a coupled model to study the inflow behavior of liquid slag to the mold-strand channel, taking the solidification of steel and slag and the periodic oscillation of mold into account. The difficulties and solutions for the simulation were described in detail. The predicted profiles of the slag rim and initial shell were in good agreement with the reports. The main results indicated that liquid slag could be squeezed out and back into the slag pool in a negative strip period while a large amount of liquid slag could infiltrate into the mold-strand channel. Thus, the amount of slag consumed in the negative strip period was relatively small compared with that in the positive strip period. The predicted variation of slag consumption during mold oscillation was periodic, and the average value was 0.274 kg/m^2 , which agreed well with the slag consumption in industrial practice. The current model can predict and optimize the oscillation parameters aiming at stable lubrication conditions.

<https://doi.org/10.1007/s11663-018-1267-y>

© The Minerals, Metals & Materials Society and ASM International 2018

I. INTRODUCTION

MOLD powder was first applied to the continuous casting (CC) of steel in 1963.^[1] The powder added on the meniscus of molten steel is expected to perform the following tasks: protect the liquid steel from oxidation, absorb floating inclusions, provide thermal insulation, lubricate the strand and control heat transfer between the mold and the solidifying shell^[2]; among these, the lubrication of the solidifying shell plays an important role, as the initial solidifying steel shell is too weak and sticky to be smoothly withdrawn from the mold.^[3] The origin of the majority of surface defects is at or within 25 mm of the meniscus in the mold.^[4,5] Thus, consistent and uniform lubrication, especially in the meniscus region during the CC process, is crucial for the smooth demolding and uniform growth of the solidifying shell and is also an essential premise for the production of defect-free casting. The lubrication is realized by the infiltration of liquid slag into the mold-strand channel, and many studies^[6–16] have been conducted to gain an understanding of the mechanism responsible for slag infiltration, as summarized in Table I.

For cold models using oil silicone,^[11] the condition tends to be isothermal whereas the conditions in the mold are not isothermal. The freezing of water as a medium simulating the slag has also been reported.^[17] However, water may be a reasonable substitute for the viscosity of steel but not for the surface and interfacial tension terms.^[1] Though adequate operational conditions could be found in high-temperature laboratory experiments^[7,18] in which the experimental apparatus contains molten steel and mold flux^[6] or low-melting Sn-5 mass pct Pb alloy and stearic acid,^[7] the inflow behavior of liquid flux into the channel could not be determined. For the description of the slag infiltration process by the approach of the mathematical model, different conclusions have been obtained even with respect to the occurrence time of slag infiltration into the mold-strand channel.^[9,10,12,16] Someone determined that the liquid slag infiltrated into the channel during the t_n period because of the increased pressure produced by a descending slag rim. While the channel became blocked because of the bending of the initial shell, others found that the flux inflow was difficult in the t_n period and could take place only during the t_p period. The above controversy may derive from the differences of the studied objects and slag properties used and the adoption of calculation assumptions (such as the neglect of top surface fluctuation, the predefined solid slag layer against the mold wall, without or with a constant shape of solid slag rim around meniscus). However, without a clear clarification of the mechanism of slag infiltration during the CC process, it is difficult to optimize the

SHAODA ZHANG, QIANGQIANG WANG, SHENGPING HE, and QIAN WANG are with the College of Materials Science and Engineering, Chongqing University, Chongqing 400044, China. Contact e-mail: wtfwaj@163.com

Manuscript submitted December, 4 2017.

Article published online April 16, 2018.

Table I. Studies on the Mechanism of Slag Infiltration

Authors	Method	Main Findings	Year	References
Kawakami <i>et al.</i>	hot experiment	the slag consumption is proportional to the t_p	1981	45
Anzai and Shigezumi	mathematical model	an early and simple model to study the inflow behavior of liquid slag to the mold-strand channel	1987	46
Tsutsumi <i>et al.</i>	cold experiment	the t_p period was an important period for the inflow behavior of mold slag	2000	7
Ojeda <i>et al.</i>	mathematical model	the slag consumption in the t_p period was proportional to the positive strip ratio during mold oscillation	2006	9
Okazawa <i>et al.</i>	mathematical model	the downward movement of the solid slag rim pushes the slag out of the meniscus region at relative high velocity	2006	10
Kajitani <i>et al.</i>	cold model	the liquid slag consumption mainly occurs in t_n , but also is positive in part of the t_p	2006	11
Lopez <i>et al.</i>	mathematical model	the slag infiltration occurs because of the opening and closing of the mold-strand channel	2010	12–14
Yang <i>et al.</i>	mathematical model and cold model	the liquid flux flows into the channel from the end of t_p to the beginning of the next t_p , including all the t_n period	2017	16
		the infiltration of mold flux is strongly governed by the channel that becomes wider in casting direction		
		the infiltration occurs as a result of shell withdrawal, mold oscillation and the pumping effect of the slag rim		
		no negative consumption was detected at any part of the oscillation cycle		
		the liquid slag is infiltrated by the negative channel pressure in the lower meniscus from the end of the t_p to the beginning of the next t_p		

t_n negative strip time when the mold is descending faster than the shell, t_p positive strip time, the rest of an oscillation cycle.

lubrication condition through casting and oscillation parameters.

These complex phenomena at the meniscus, such as rapid heat transfer, level fluctuation, formation and slag rim, *etc.*, make it difficult to determine the infiltration mechanism through industrial trials and laboratory experiments. With the advent of faster computers and advanced numerical models, more and more eminent researchers^[19–21] emphasize that mathematical modeling is a remarkable tool and can accurately simulate the mechanisms responsible for various defects and literally allow us to ‘see’ what is happening in the mold. Thus, the current study preferred an approach of numerical simulation with a two-dimensional (2D) model that focuses on the inflow behavior of slag in the mold-strand channel based on the CC process of low-carbon steel with specialized mold powder. The difficulties of and solutions for the simulation are described in detail in Section II followed by the validation of models in Section III. Finally, the evolution of some related transport phenomena during mold oscillation, such as the inflow of liquid slag, distribution of pressure at the meniscus, variation of slag film thickness and predicted slag consumption, is presented in Section IV.

II. MATHEMATICAL FORMULATION

A. Models Used

For the multi-phase simulation, the fluid model was based on the solution of the Navier-Stokes equations for incompressible viscous flow. The effect of turbulence was added through the renormalization group (RNG)

k - ϵ model, which could provide an analytically derived differential formula for effective viscosity that accounts for the low Reynolds number effects^[22] and has been proven to be fast and robust.^[23,24] The volume of fluid (VOF) method^[25] was employed to track the steel-slag and the gas-slag interfaces. In the current study, the surface tension effect among phases was taken into account using the continuous surface force (CSF) model,^[26,27] which interpreted the surface tension as a continuous effect across an interface rather than as a boundary value condition on the interface. For the solidification model, the enthalpy-porosity technique^[28] was used to track the liquid-solid front. The mathematical models above have been described in previous work.^[29,30]

B. Calculation Strategy and Solution Method

To settle the difficulties in convergence during the multi-phase modeling, the following calculation strategy was designed. First, equations were solved to obtain the velocity field of multiphase flow using the RNG k - ϵ model and under isothermal conditions. After a stable flow pattern was reached, approximately 20 seconds of calculation time, the solidification model was solved. Meanwhile, the copper mold plate oscillation was activated through the method of dynamic mesh, which could deal with the problem with boundary motion, and the motion velocity of the oscillating mold was applied with user-developed subroutines. Due to the obvious difference of density between the slag and gas, the magnitude of velocity within the gas phase and near the corner of the slag-gas mold was much larger than

that of other positions, easily causing a divergence in the calculation. To deal with this problem, an adequate reduction of the relaxation factor and time step was needed. Then, after several seconds of steady modeling, the time step could be enhanced from 0.00001 to 0.0001 seconds to improve the calculation speed. The calculation was considered to be stable when the distribution of liquid and solid slag film and the solidified shell did not obviously vary.

For the solution methods, the discretized equations were solved for velocity and pressure by the Pressure-Implicit with Splitting of Operators scheme,^[22] which was highly recommended for all transient flow calculations. To speed up the transient simulation, the non-iterative time-advancement (NITA) scheme was employed, which preserved the overall temporal accuracy. The NITA scheme does not need the outer iterations, performing only a single outer iteration per time step. The current multi-phase coupling simulation took approximately 3 weeks using an Intel(R) Xeon(R) E3-1240 v5 CPU (process base frequency: 3.5 GHz; memory size: 32 GB) with the computational fluid dynamics codes FLUENT 14.0.^[22]

C. Mesh System

Considering the computational resource, the study adopted a 2D calculation domain. Figure 1 shows half of the geometric model, which corresponds to the center plane parallel to the broad face. The domain consists of a submerged entry nozzle (SEN) with 15 deg downward angle and 180 mm submergence depth, molten steel of total 1.4 m below the meniscus, slag pool of 50 mm thickness, air phase and solid mold copper plate of 900 mm height and 20 mm thickness. The initial meniscus was 100 mm below the mold top.

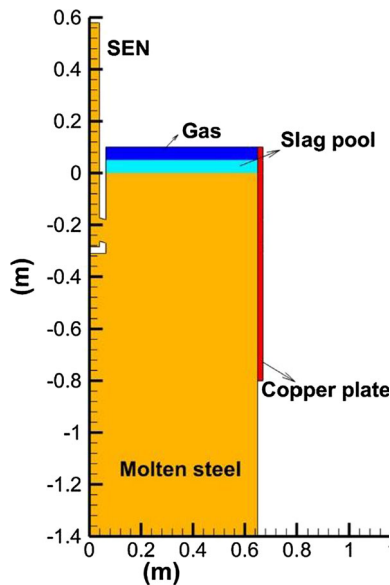


Fig. 1—Schematic of the calculation domain.

To accurately capture the inflow behavior of the liquid flux and the subtle variation of slag film thickness, the domain adjacent to the mold side was enhanced with a mesh boundary layer in which the minimum cell size, growth factor of the adjacent mesh and total depth were 50 μm , 1.03 and 30.4 mm, respectively, as shown in Figure 2. The total number of structured grids for the established model was approximately 200,000. An elaborate design of mesh is of significance for the reproduction of the phenomena of interest, especially for some subtle variations.^[14]

D. Boundary Condition

1. Domain containing molten steel

The 2D domain allows the use of an extremely fine mesh and makes the prediction of slag infiltration possible with reasonable run times. However, the determination of the inlet velocity of SEN required much attention. For the three-dimensional (3D) simulation model, the inlet velocity could be calculated based on the mass conservation. Actually, the SEN locates in the cavity of the mold, and its external diameter is smaller than the cavity thickness of the mold, which means that any individual plane parallel to the broad face cannot fully reflect the flow pattern within the mold. Thus, if the value of inlet velocity derived from the 3D model is directly applied in the 2D model, the velocity at the inlet of the 2D domain will be overestimated. To reduce the loss of accuracy, the current study first developed a 3D model with a single phase of molten steel, and then the velocity components along the center line of the nozzle port were obtained. Finally, the value of the inlet velocity of the 2D model was changed, and the obtained distribution of velocity at the nozzle port was compared with that of the 3D simulation. Figure 3 shows the comparison of velocity components at the nozzle port between the 2D and 3D results. It can be seen that when the inlet velocity of the 2D model is 0.78 m/s, the calculated distribution of the velocity components basically agrees with that of the 3D results at a casting speed of 0.9 m/min. The difference in velocity might result from the effect of fluid flow along the mold thickness.

At the bottom of the calculation domain, the fully developed flow condition was adopted, and normal gradients of all dependent variables were assumed to be zero.^[31] The superheat of molten steel at the inlet was 20 K. For the region below the mold, the heat transfer on the narrow surface of the strand was defined by Eq. [1], and the spray-cooling heat-transfer coefficient h_{spray} ($\text{W}/(\text{m}^2 \times \text{K})$) was calculated using Eq. [2].^[32]

$$q_s = h_{\text{spray}}(T_{\text{slab}} - T_{\text{spray}}) \quad [1]$$

$$h_{\text{spray}} = 0.581 W^{0.451} (1 - 0.0075 T_{\text{spray}}) \quad [2]$$

where q_s is the heat flux on the surface (W/m^2), T_{slab} is the surface temperature of strand (K), T_{spray} is the temperature of the spray-cooling water (300 K), and W is the water flow rate (240 l/min).

2. Domain containing the gas and slag pool

The top surface of the gas phase was set as the free-slip wall at constant temperature (300 K). To distinguish the liquid slag layer from the solid slag layer (or sintered layer), several studies^[12,33] applied the fact that the temperature below which there was a marked increase in viscosity due to the precipitation of crystals was referred to as the break temperature, T_b . In the current study, the slag is made up of 34.60 pct SiO₂, 4.83 pct Al₂O₃, 0.85 pct Fe₂O₃, 31.22 pct CaO, 2.32 pct MgO, 6.96 pct F and 9.02 pct R₂O of the mass, which is designed for the slab CC of low-carbon steel. The basicity and melting point are 0.9 and 1382 K (1107 °C), respectively. The measurement of slag viscosity was carried out using the rotating cylinder method, according to Chinese industrial standards (YB/T 185-2001). The specific steps of the viscosity measurement are outlined in Reference 34. The viscosity-temperature result obtained by the laboratory experiment is plotted in Figure 4. During the cooling process, the slag viscosity first increased gradually. Then, the slag viscosity grew larger in a short temperature range at approximately 1358 K (1085 °C). When the test temperature was below 1352 K (1079 °C), the slag viscosity rose sharply. Thus, the current simulation took the break temperature of the slag as 1352 K (1079 °C). The fitting equation for the variation of viscosity as a function of temperature is listed in Table II. It is well known that the mold powder fed onto the meniscus of molten steel first forms a sinter layer, then a mushy layer and eventually a liquid flux pool.^[35,36] However, for calculation simplicity, only the effect of the solid slag rim sticking to the copper plate on the slag infiltration was considered in the current simulation.

3. Solid domain

The oscillation of the mold was realized using the method of dynamic mesh, by which the copper plate was regarded as a rigid body, and its oscillation velocity was derived by:^[37]

$$v_m = 2\pi Af \cos(2\pi ft) \quad [3]$$

where v_m is the oscillation velocity of the mold (m/s) at time t (seconds), A is the amplitude (m), and f is the oscillation frequency (Hz).

The amount of heat extracted by the water-cooling copper plate is defined by the heat transfer coefficient of the cold face and was given by:^[12,15]

$$h_{\text{mold}} = \frac{\left[0.023 \left(\frac{\rho_w u_w D}{\mu_w} \right)^{0.8} \left(\frac{C_w \mu_w}{\lambda_w} \right)^{0.4} \right] \lambda_w}{D} \quad [4]$$

where h_{mold} represents the convective heat transfer coefficient of cooling water (W/(m² × K)), λ_w represents the thermal conductivity coefficient of cooling water (0.62 W/(m × K)), D is the equivalent diameter of the water channel (0.008 m), μ_w represents the viscosity of cooling water (0.00085 Pa·s), ρ_w is the density of cooling water (1000 kg/m³), C_w is the specific heat capacity (4182 J/(kg × K)), and u_w is the calculated flow velocity

of cooling water (~ 7.88 m/s) when the water flow rate for the narrow copper plate is 520 l/min.

Besides the determination of the motion and heat transfer for the mold, the contact area between the fluid and the solid was set as the type of ‘interface’ through which the kinetic and thermal energy can mutually transmit.^[22] The gap formed between the mold and the solid slag film, especially in the lower part of the mold, would cause additional thermal resistance. The value of the interface thermal resistance was reported to be related to the solidification temperature of the mold flux^[8] or slag basicity.^[14] Taking the ferrostatic pressure on the shell into account, the study of Hanao^[38] concluded that the interfacial resistance value was 0.0004 (m² × K)/W based on the measurements of the heat flux and the slag rim from the mold. As the uncertain distribution of gap thickness along the withdrawal direction, the magnitude of interface thermal resistance was set as a constant of 0.0002 (m² × K)/W in the current study.

The details of the casting and physical property parameters used in the current study are listed in Tables II and III, respectively.

III. VALIDATION OF MODELS

To validate the models established in the current study, the calculated profiles of the slag rim and initial shell were compared to the results in References 8, 39 and 40. Figure 5 demonstrates the comparison of the slag rim between the prediction and the sample taken from the meniscus of a plant mold casting low-carbon steel.^[8] It can be seen that both had a well-developed bulge on the upper part of the slag rim. It should be pointed out that as only the liquid slag was considered, the obtained slag rim in Figure 5(a) was larger in the vertical direction, resulting in a thick tip at the upper slag rim. Though not explicitly stated in Reference 8, the well-developed sample in Figure 5(b) might be taken in the tail-out period. Thus, both are in good agreement in terms of general shape.

The profile of the upper meniscus, *i.e.*, the initial shell, was often expressed by the Bikerman equation^[39,41] below, which considered the interfacial tension and the densities of slag and molten steel.

$$x - x_0 = -\sqrt{2a^2 - z^2} + \frac{a}{\sqrt{2}} \ln \frac{a\sqrt{2} + \sqrt{2a^2 - z^2}}{z} \quad [5]$$

$$x_0 = a - \frac{a}{\sqrt{2}} \ln(\sqrt{2} + 1) \quad [6]$$

$$a = \sqrt{\frac{2 \cdot \Delta\gamma}{\Delta\rho \cdot g}} \quad [7]$$

where x is the distance perpendicular to the mold wall (m), z is the distance along the mold wall (m), g is the

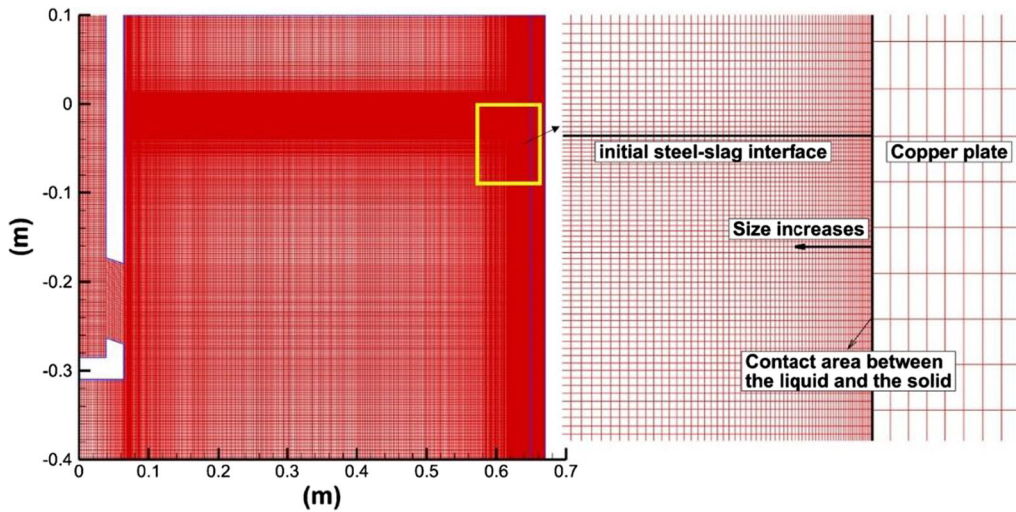


Fig. 2—Mesh system for the calculation domain.

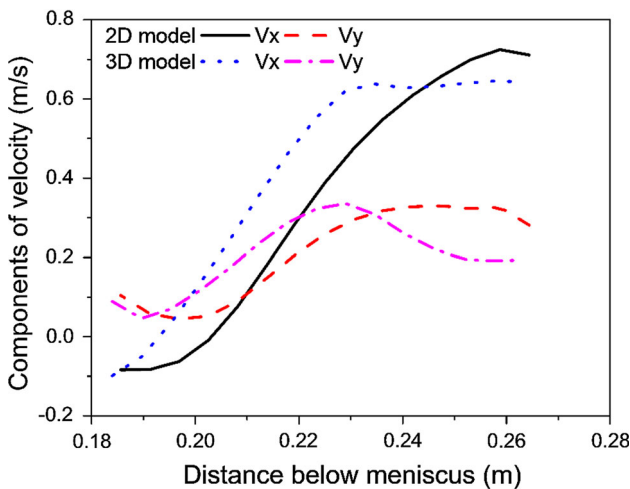


Fig. 3—Comparison of velocity at the nozzle port between the 2D and 3D simulations.

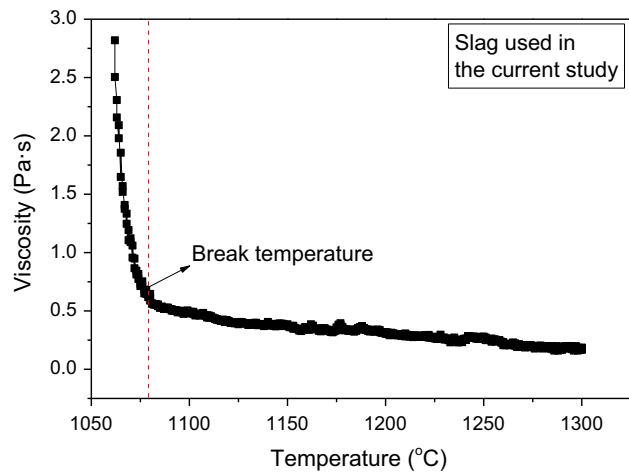


Fig. 4—Viscosity of the mold slag as a function of temperature.

Table II. Dimensions and Casting Parameters for the Simulation

Parameter	Value	Parameter	Value
Mold Width, mm	1300	height of copper plate, mm	900
Sen Port Angle	15 deg down	thickness of copper plate, mm	20
Outlet Width × Height, mm × mm	70 × 90	region below the mold exit, mm	500
Nozzle Inner Diameter, mm	78	h_{mold} , W/(m ² × K)	28,216
SEN Submerged Depth, mm	180	h_{spray} , W/(m ² × K)	1332
Casting Speed, m/min	0.9	interfacial resistance, (m ² × K)/W	0.0002
Superheat, K	20	mold oscillation	sinusoidal
Surface Tension of Slag-Gas, N/m	0.8	frequency, Hz	2
Surface Tension of Steel-Slag, N/m	1.3	amplitude, m	0.003

gravitational acceleration (9.81 m/s^2), and $\Delta\gamma$ (N/s) and $\Delta\rho$ (kg/m^3) are the difference of surface tension and density between molten steel and liquid slag, respectively. The calculated meniscus shape for the parameters in Tables II and III are presented in Figure 6.

The calculated profile presents a round and smooth interface. Figure 7 presents the profiles of the initial shell (with the liquid fraction of molten steel < 0.7) when the copper plate reaches the highest level and then the lowest level during an oscillation cycle. Overall, the surface of the newly formed shell close to the slag film

Table III. Physical Property Parameters Used in the Current Study

Phase	Parameter	Value
Steel	density, kg/m ³	7400
	viscosity, kg/(m·s)	0.0067
	heat capacity, J/(kg·K)	750
	thermal conductivity, W/(m·K) ^[15]	$13.86 + 0.01113 \times (T - 273.15)$
	latent heat, J/kg	270,000
	liquidus temperature, K	1805
Slag	solidus temperature, K	1783
	density, kg/m ³	2500
	viscosity, kg/(m·s)	$= -0.00152 \times (T - 273) + 2.14, T > T_b$ $= -0.11152 \times (T - 273) + 120.60, 1335 \text{ K} < T < T_b$ $= 3.0, T < 1335 \text{ K}$
	break temperature, T_b , K	1352 (1079 °C)
Mold ^[12,13]	thermal conductivity, W/(m·K) ^[15]	2.0, $T \geq T_b$; 1.2, $T < T_b$
	heat capacity, J/(kg·K) ^[2]	830
	density, kg/m ³	8973
	heat capacity, J/(kg·K)	390
	thermal conductivity, W/(m·K)	387

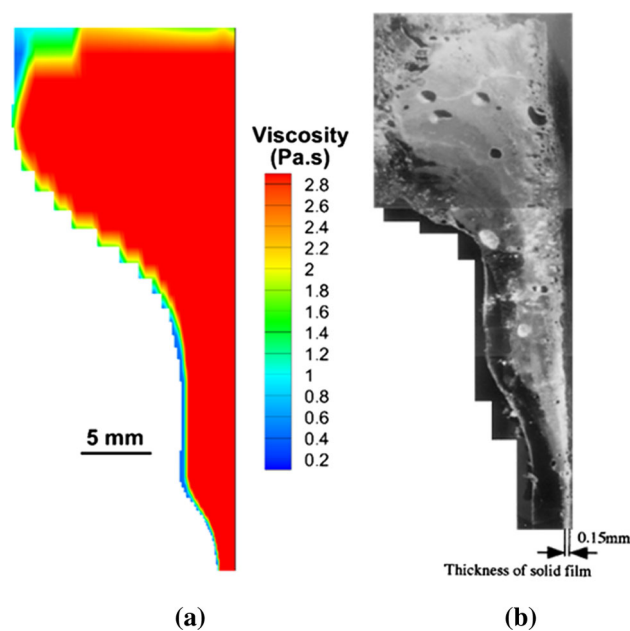


Fig. 5—Comparison of the slag rim between the prediction and the sample from industrial practice. (a) Calculated slag rim and (b) slag rim sample Ref. [8] (permission granted by ISIJ International, reprinted).

side is relatively even, while the shell's internal surface is 'sausage' shaped. It is interesting to note that as the copper plate travelled downwards with a time lapse of 0.25 seconds, the initial shell grew, bending toward the steel bulk, which shed light on the formation of the initial shell being not only dependent on the interfacial tension between the steel and slag, but also on some specific conditions, such as mold oscillation, rapid heat extraction and a complicated interplay of forces. For ultra-low carbon steel, which is susceptible to under-cooling relative to other steel grades, the meniscus may freeze suddenly to extend the solidifying shell tip. If the frozen meniscus is retained, then the oscillation mark forms on the shell surface.^[41] In short, the

mentioned good agreements indicate the accuracy of the established models in the study.

IV. PHENOMENA DURING SLAG INFILTRATION

A. Inflow Behavior of Liquid Slag

To understand the inflow characteristics of liquid slag in the vicinity of the meniscus, the study set six specific moments within a cycle for the sinusoidal oscillation, as shown in Figure 8. The t_n during which the mold moves downward faster than the casting speed ($v_c = 0.015 \text{ m/s}$) is approximately 0.186 seconds. The oscillation amplitude is 3 mm, and the positive one at the mold displacement curve means that the mold locates above the initial position.

Figure 9 visualizes the transients of the slag rim, velocity vectors of the liquid slag and steel at the mold corner region, corresponding to the specific moments in Figure 8. The domain of liquid slag, which was blanketing to simplify the description, formed a channel that ran from the slag pool to the mold-strand gap. At t_1 , the mold was on the upstroke and at the initial position. It can be seen that much of liquid slag could infiltrate down into the channel, and the liquid slag near the slag rim went up, which might be affected by the high-speed upward copper plate. At t_2 , the mold reached the top with zero velocity, when the channel width was obviously larger than that at t_1 , and liquid slag could smoothly flow into the channel. Subsequently, the oscillation velocity gradually increased and entered into the t_n period. At t_3 , a small-scale backflow formed at the upper meniscus and impacted on the initial shell. The mold was on the downstroke and went back to the initial position in the middle of the oscillation cycle at t_4 . To some extent, as the solid slag rim moved down with the copper plate, it acted like a piston^[42] and occupied the space of liquid slag. Thus, it is clearly shown that much of the liquid slag was squeezed out from the channel and back into the slag pool. At the

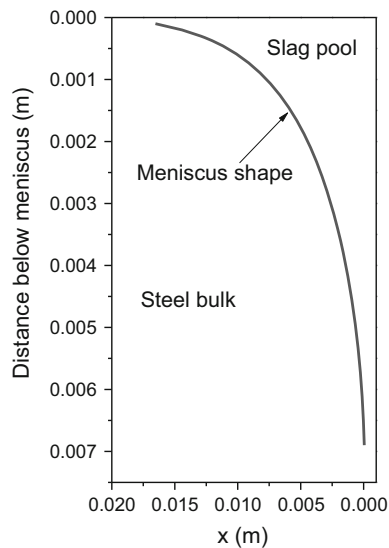


Fig. 6—Meniscus shape based on the Bikerman equation.

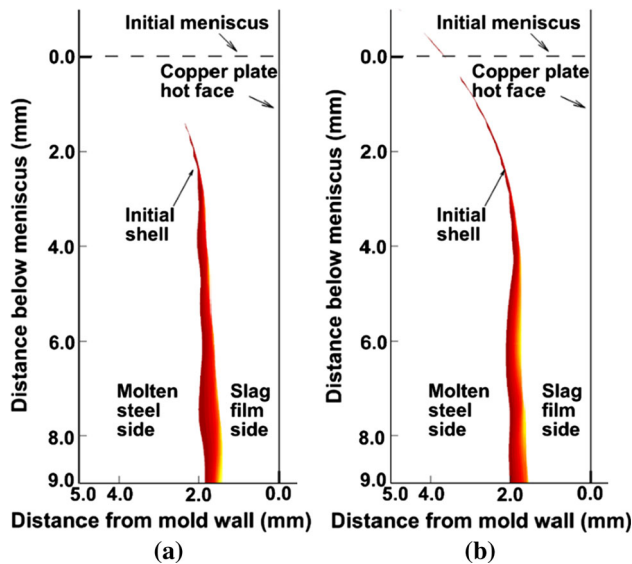


Fig. 7—Profiles of the initial shell with different positions of the oscillating mold. (a) Mold at the highest level and (b) mold at the lowest level.

same time, the variation of the liquid slag flow also exerted some disturbance on the shell tip. At the later stage of t_n (Figure 9(e)), the trend of the liquid slag flowing back into the slag pool became weak; there was still much liquid slag that could flow into the channel and lubricate the solidifying shell. At t_6 , the mold was at the lowest position with zero velocity. Though the channel width was narrower than that at t_2 , the liquid slag could smoothly flow into the channel.

Figure 10 demonstrates the distribution of pressure in the flux channel. At the beginning, the maximum was approximately 1410 Pa at the upper meniscus, and the pressure was lower than 1350 Pa at the lower meniscus. As the mold oscillated from the t_p to the t_n , the pressure in the channel increased, especially for the lower part. At

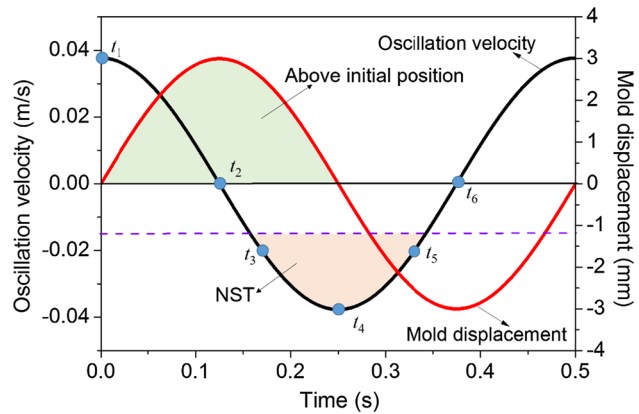


Fig. 8—Mold velocity and displacement within an oscillation cycle.

the middle of the t_n period (Figure 10(d)), the area with over 1650 Pa was the largest. During the rest of the oscillation cycle, the pressure along the channel decreased gradually, which presented periodic pressure variation in a cycle. The relative motion between the copper plate and the initial shell generated varying pressure in the flux channel, which was related to the slag infiltration during each oscillation cycle.

Figures 9 and 10 also elucidate that the shapes of the slag rim and the initial shell tip actually varied during mold oscillation. Thus, the idealization of the initial shell profile by the Bikerman equation and the hypothesis of the slag rim with a constant shape may yield unnecessary deviation in the in-depth analysis of the infiltration mechanism of liquid slag.

For further analysis of the inflow behavior of liquid slag, the study set two monitoring points at the entrance of the mold-strand channel, Point M-1 (x coordinate 0.647, y coordinate 0) was near the initial shell, and point M-2 (x coordinate 0.648, y coordinate 0) was close to the slag rim. Figure 11 shows the variation of the velocity components as a function of the oscillation cycle. In the current studied coordinate system, the positive value of V_x denotes that the velocity component of liquid slag points to the side of solid slag, and the positive value of V_y denotes that the velocity component is opposite to the withdrawal direction. The t_n period was taken as the focus, during which V_x and V_y for point M-1 were negative and positive, respectively, and were both negative for point M-2. Figure 10(b) indicates that during the t_n period the liquid slag at point M-1 flows toward the slag pool, while the liquid slag at point M-2 flows into the mold-strand channel. Thus, to judge the occurrence time of slag infiltration, the analysis of an individual monitoring point could easily lead to the opposite conclusion compared with the qualitative results in Figure 9.

B. Heat Flux and Slag Film Thickness

The evolution of heat flux at a point 45 mm below the meniscus and on the hot copper plate surface, and the thickness variation of slag film at the same height, are plotted in Figure 12. For an oscillation cycle, the heat flux of the monitoring point presented an

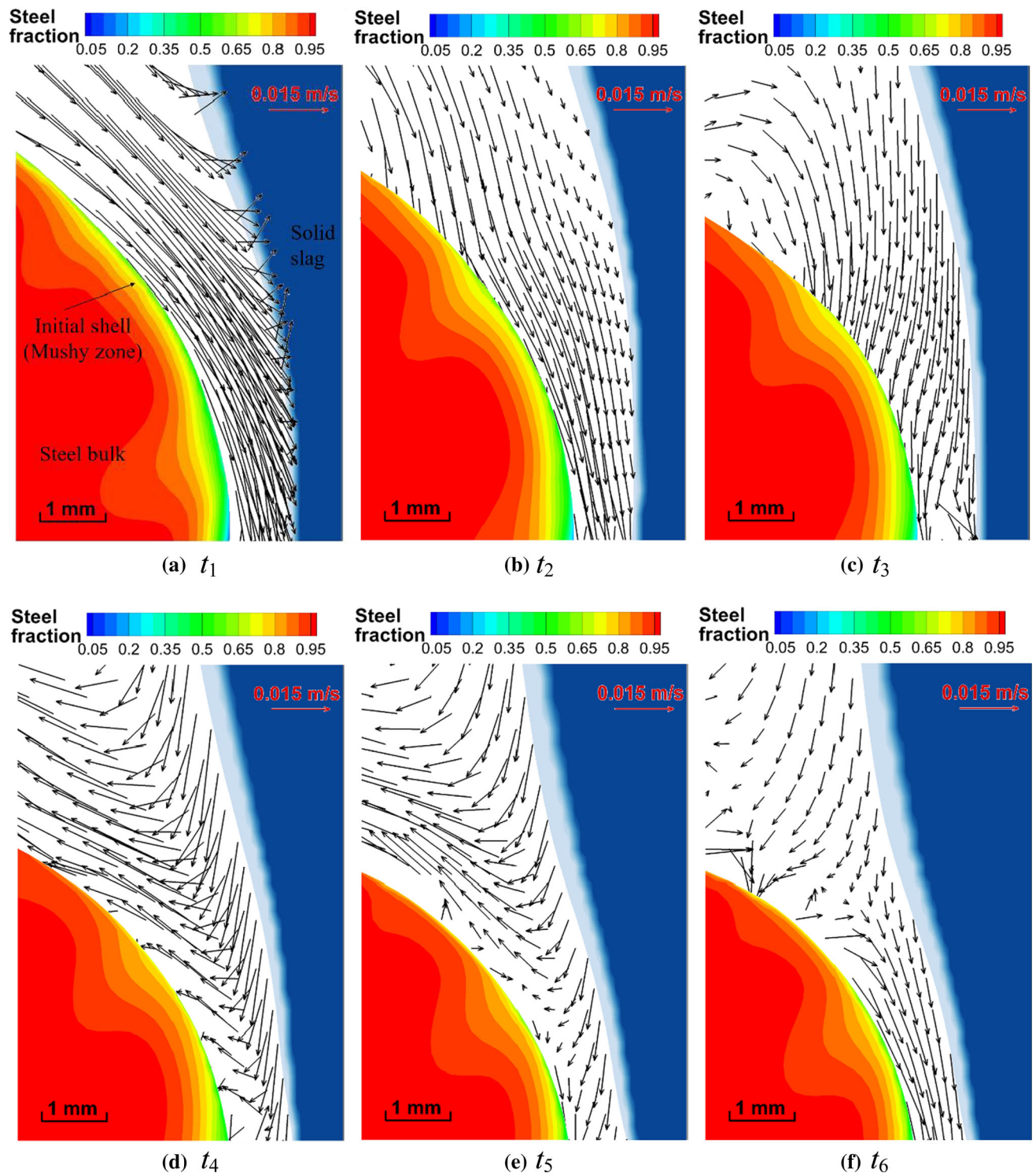


Fig. 9—Transients of the inflow of liquid slag into the mold-strand channel. (a) t_1 , (b) t_2 , (c) t_3 , (d) t_4 , (e) t_5 and (f) t_6 .

increasing trend in the first t_p period and became the peak just before the start of t_n . Then, the heat flux decreased gradually, including the whole t_n stage and most of the following t_p . The heat flux reached the minimum value and showed an increasing trend before the start of the next oscillation cycle. The thickness

variation of solid slag film (d_s) revealed that d_s first increased and then reduced, reaching a minimum at the middle of t_n . The d_s increased again in the rest of the t_n period and finally reached a maximum value in the early stage of the next t_p period. It is obvious that the behavior of the liquid layer thickness (d_l) is a mirror

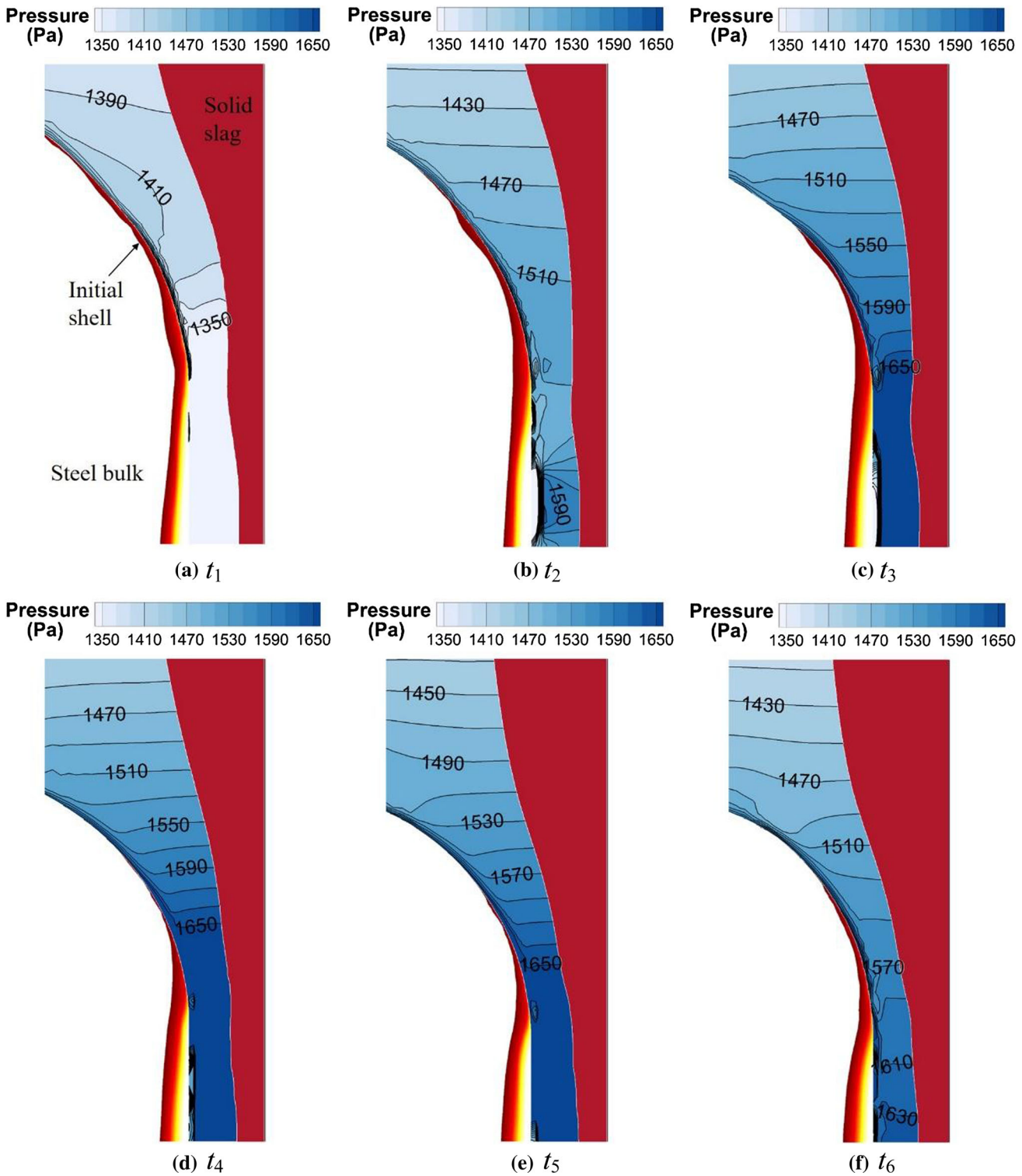


Fig. 10—Distribution of pressure in the flux channel. (a) t_1 , (b) t_2 , (c) t_3 , (d) t_4 , (e) t_5 and (f) t_6 .

image of the solid slag film, which implies that the liquid film grows at the expense of the solid film, in line with the study of Lopez.^[12] The calculated total thickness of slag film in the current study was approximately 1.45 mm, which basically accords with the calculated results in Reference 8.

C. Slag Consumption

Lubrication is directly correlated with the slag consumption, which is also related to the thickness of liquid film. As revealed in Reference 43, d_1 varied along the casting direction. Thus, to achieve quantitative results of slag

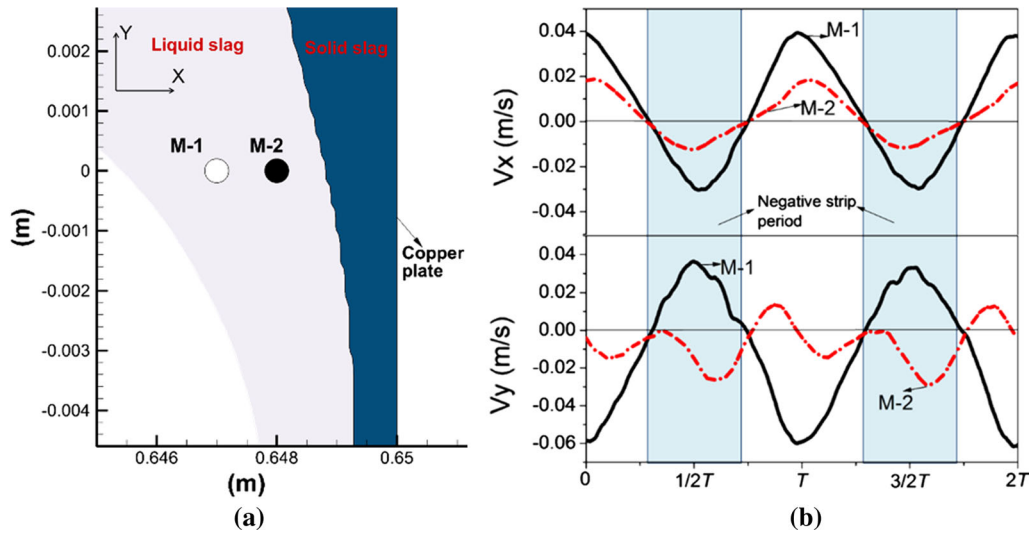


Fig. 11—Monitoring of velocity components at the entrance of the mold-strand channel. (a) Position of monitoring points and (b) change of velocity components.

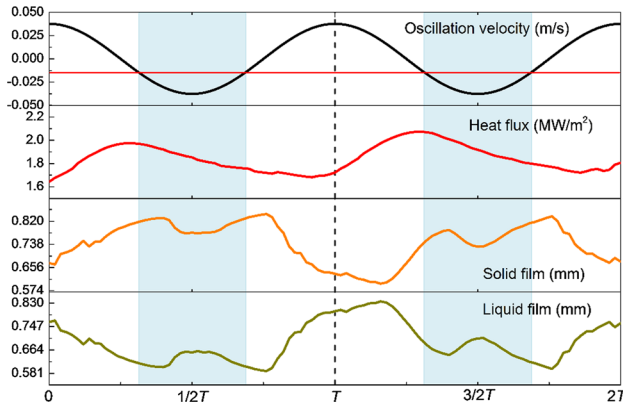


Fig. 12—Evolution of heat flux and thickness of slag film at the position of 45 mm below the meniscus.

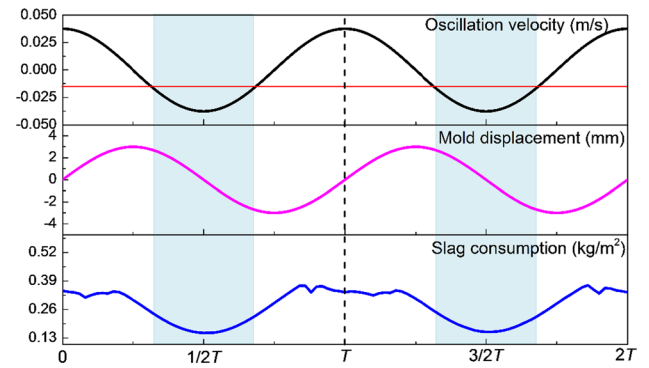


Fig. 13—Evolution of slag consumption with mold oscillation velocity and displacement.

consumption during mold oscillation, the mass conservation was applied according to the thickness and the equivalent velocity of liquid film at the position of 300 mm below the meniscus, as the calculated length of liquid film along the withdrawal direction was approximately 600 mm. The current study treated the slag consumption as Q_s in kilograms of powder per square meter of strand (kg/m^2). Figure 13 shows the evolution of the slag consumption with the mold oscillation. At the beginning, the mold was on the upstroke with maximum speed, and the calculated transient Q_s was approximately $0.350 \text{ kg}/\text{m}^2$. Within a time lapse of 0.1 seconds, Q_s decreased first and then increased, and it fluctuated at the level of $0.320 \text{ kg}/\text{m}^2$. After that, Q_s decreased steadily until it reached a minimum at the half of the cycle, when the mold was in the middle of t_n . Subsequently, Q_s increased steadily, and shortly after the mold entered into the next t_p , Q_s rose to approximately $0.375 \text{ kg}/\text{m}^2$. Finally, Q_s fluctuated at a high level until the end of the current oscillation cycle. For the next cycle, the

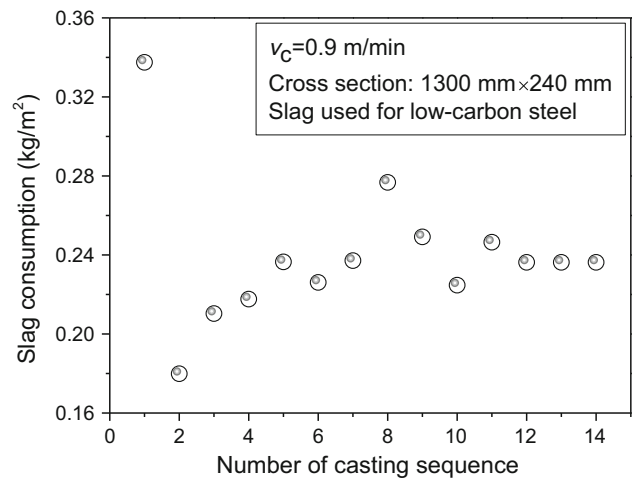


Fig. 14—Slag consumption of 14 casting sequences.

variation of Q_s had a trend similar to the above one. The calculated average slag consumption in each oscillation cycle was approximately 0.274 kg/m^2 .

The powder consumption in industrial practice could be easily obtained by dividing the total weight of steel in each ladle by the mass of mold power consumed (Q_t , kg/ton). To make a comparison, the powder consumption is expressed as the following way^[44]:

$$Q_t = R^* Q'_s / (7.4 f^*) \quad [8]$$

where R^* = (surface area/volume) of mold and equals the value of $2 \times (1.3 + 0.24)/(1.3 \times 0.24)$, f^* is the loss on ignition of the mold powder (0.85 in this study), 7.4 is the density of steel in ton/m^3 , and Q'_s is the consumed powder that participates in the lubrication (kg/m^2). The actual slag consumption for 14 casting sequences is plotted in Figure 14, in which the slag consumption differed from each casting sequence and varied from 0.180 to 0.337 kg/m^2 , which agrees well with the prediction in Figure 13.

V. CONCLUSIONS

A two-dimensional multi-phase model was established to study the infiltration of liquid slag into the mold-strand channel during the low-carbon steel CC process. The conclusions can be summarized as follows:

- (1) The study compared the profiles of the slag rim and initial shell between the prediction and measurements and the calculated quantitative slag consumption with the actual slag consumption. The good agreement indicated that the model established was reasonable and able to predict the lubrication condition during the CC process.
- (2) The downward motion of the slag rim, especially in the t_n period, could push some liquid slag out and increase the pressure at the lower part of the meniscus. Thus, the amount of slag consumed in t_n was relatively small compared with that in t_p .
- (3) The predicted variation of slag consumption presented a periodic trend during mold oscillation, and the minimum was reached at the middle of the t_n period. The calculated slag consumption was approximately 0.274 kg/m^2 and was in line with the industrial slag consumption. Thus, the current model could be employed to predict and optimize the oscillation parameters.
- (4) The inflow of liquid slag in the vicinity of the meniscus is determined by many complex factors; the simplified initial shell profile by the Bikerman equation and the slag rim with constant shape could yield an unnecessary deviation in an in-depth analysis of the infiltration mechanism of liquid slag.

ACKNOWLEDGMENTS

The authors are grateful for support from the Key Project of Natural Science Foundation of China

(Grant No. U1660204) and the Fundamental Research Funds for the Central Universities in China (Grant No. 106112017CDJXY130001).

REFERENCES

1. K.C. Mills: *Ironmak. Steelmak.*, 2017, vol. 44, pp. 326–32.
2. K.C. Mills: *ISIJ Int.*, 2016, vol. 56, pp. 1–13.
3. K. Okazawa, T. Kajitani, W. Yamada, and H. Yamamura: *ISIJ Int.*, 2006, vol. 46, pp. 226–33.
4. V. Ludlow, B. Harris, S. Riaz, and A. Normanton: *Ironmak. Steelmak.*, 2005, vol. 32, pp. 120–26.
5. Y. Ren, L.F. Zhang, and S.S. Li: *ISIJ Int.*, 2014, vol. 54, pp. 2772–79.
6. N. Pradhan, M. Ghosh, D.S. Basu, and S. Mazumdar: *ISIJ Int.*, 1999, vol. 39, pp. 804–08.
7. K. Tsutsumi, J. Ohtake, and M. Hino: *ISIJ Int.*, 2000, vol. 40, pp. 601–08.
8. A. Yamauchi, T. Emi, and S. Seetharaman: *ISIJ Int.*, 2002, vol. 42, pp. 1084–93.
9. C. Ojeda, J. Sengupta, B.G. Thomas, J. Barco, and J.L. Arana: *Proc. AISTech Conf.*, 2006, pp. 1017–28.
10. K. Okazawa, T. Kajitani, W. Yamada, and H. Yamamura: *ISIJ Int.*, 2006, vol. 46, pp. 234–40.
11. T. Kajitani, K. Okazawa, W. Yamada, and H. Yamamura: *ISIJ Int.*, 2006, vol. 46, pp. 250–56.
12. P.E. Ramirez-Lopez, P.D. Lee, and K.C. Mills: *ISIJ Int.*, 2010, vol. 50, pp. 425–34.
13. P.E. Ramirez-Lopez, P.D. Lee, K.C. Mills, and B. Santillana: *ISIJ Int.*, 2010, vol. 50, pp. 1797–1804.
14. P.E. Ramirez-Lopez, U. Sjoström, P.D. Lee, K.C. Mills, B. Jonsson, and J. Janis: *Proc. AISTech Conf.*, 2012, pp. 1259–67.
15. X.D. Wang, L.W. Kong, M. Yao, and X.B. Zhang: *Metall. Mater. Trans. B.*, 2017, vol. 48B, pp. 357–66.
16. J. Yang, X.N. Meng, N. Wang, and M.Y. Zhu: *Metall. Mater. Trans. B.*, 2017, vol. 48B, pp. 1230–47.
17. M.S. Jenkins: Monash University, 1999.
18. K. Tsutsumi, H. Murakami, S. Nishioka, M. Tada, M. Nakada, and M. Komatsu: *Tetsu-to-Hagane.*, 1998, vol. 84, pp. 617–24.
19. K.C. Mills, P.E. Ramirez-Lopez, P.D. Lee, B. Santillana, B.G. Thomas, and R. Morales: *Ironmak. Steelmak.*, 2014, vol. 41, pp. 242–49.
20. B.G. Thomas and L.F. Zhang: *ISIJ Int.*, 2001, vol. 41, pp. 1181–93.
21. L.F. Zhang: *JOM.*, 2012, vol. 64, pp. 1059–62.
22. ANSYS FLUENT 14.0. Canonsburg, PA: ANSYS, Inc, 2011.
23. Q. Yuan, S.P. Vanka, B.G. Thomas, and S. Sivaramakrishnan: *Metall. Mater. Trans. B.*, 2004, vol. 35B, pp. 967–82.
24. P.E. Ramirez-Lopez, K.C. Mills, P.D. Lee, and B. Santillana: *Metall. Mater. Trans. B.*, 2012, vol. 43B, pp. 109–22.
25. C.W. Hirt and B.D. Nichols: *J. Comput. Phys.*, 1981, vol. 39, pp. 201–25.
26. J.U. Brackbill, D.B. Kothe, and C. Zemach: *J. Comput. Phys.*, 1992, vol. 100, pp. 335–54.
27. P. Liovic, J. Liow, and M. Rudman: *ISIJ Int.*, 2001, vol. 41, pp. 225–33.
28. L.F. Zhang and Y.F. Wang: *JOM.*, 2012, vol. 64, pp. 1063–74.
29. Q.Q. Wang and L.F. Zhang: *Metall. Mater. Trans. B.*, 2016, vol. 47B, pp. 1933–49.
30. Q.Q. Wang, L.F. Zhang, and S. Sridhar: *Metall. Mater. Trans. B.*, 2016, vol. 47B, pp. 2623–42.
31. S.W. Lei, J.M. Zhang, X.K. Zhao, and K. He: *ISIJ Int.*, 2014, vol. 54, pp. 94–102.
32. R.D. Morales, A.G. Lopez, and I.M. Olivares: *ISIJ Int.*, 1990, vol. 30, pp. 48–57.
33. Y. Meng and B.G. Thomas: *Metall. Mater. Trans. B.*, 2003, vol. 34B, pp. 707–25.
34. T. Wu, S.P. He, L.L. Zhu, and Q. Wang: *Mater. Trans.*, 2016, vol. 57, pp. 58–63.
35. K.C. Mills, A.B. Fox, R.P. Thackray, and Z. Li: *VII Int. Conf. Molten Slags Fluxes Salts*, 2004, pp. 713–21.
36. Y. Ren, L.F. Zhang, H.T. Ling, Y. Wang, D.T. Pan, Q. Ren, and X.C. Wang: *Metall. Mater. Trans. B.*, 2017, vol. 48B, pp. 1433–38.

37. X.K. Li, C.S. Qiao, X.S. Xu, H. Zhong, C.L. Xu, and S.C. Gong: *Iron Steel*, 1992, vol. 27, pp. 20–24.
38. M. Hanao, M. Kawamoto, and A. Yamanaka: *ISIJ Int.*, 2012, vol. 52, pp. 1310–19.
39. J.J. Bikerman: *Physical surfaces*, Academic Press, Cambridge, 1970.
40. H. Fredriksson and J. Elfsberg: *Scand. J. Metall.*, 2002, vol. 31, pp. 292–97.
41. H. Shin, S. Kim, B.G. Thomas, G. Lee, J. Park, and J. Sengupta: *ISIJ Int.*, 2006, vol. 46, pp. 1635–44.
42. K.C. Mills and Carl-Åke Däcker: *The casting powders book*, Springer, New York, 2017.
43. Y. Meng: Ph.D. Thesis, University of Illinois, 2004, p. 179.
44. K.C. Mills, A.B. Fox, Z. Li, and R.P. Thackray: *Ironmak. Steelmak.*, 2005, vol. 32, pp. 26–34.
45. K. Kawakami, T. Kitagawa, H. Mizukami, H. Uchibori, S. Miyahara, M. Suzuki, and Y. Shiratani: *Tetsu-to-Hagane.*, 1981, vol. 67, pp. 1190–99.
46. E. Anzai and T. Shigezumi: Nippon Kokan Technical Report, 1987, vol. 34, pp. 31–40.